Integrative Biology

Accepted Manuscript

ROYAL SOCIETY OF CHEMISTRY

www.rsc.org/ibiology

An individual based computational model of intestinal crypt fission and its application to predicting unrestrictive growth of the intestinal epithelium

Carmen Pin[1*], Aimee Parker[1], A. Patrick Gunning[2], Yuki Ohta [3], Ian T. Johnson[2], Simon R. Carding[1,4] and Toshiro Sato[3]

[1]Gut Health and Food Safety Research Programme, [2]Food and Health Research Programme, Institute of Food Research, Norwich. NR4 7UA. UK
[3]School of Medicine, Keio University, Shinjuku-ku, Tokyo 160-8582 Japan
[4]Norwich Medical School, University of East Anglia, Norwich. NR4 7TJ. UK.

[*]Corresponding author:
carmen.pin@ifr.ac.uk
Tel: +441603255000
Fax: +441603507723

Abstract

Intestinal crypt fission is a homeostatic phenomenon, observable in healthy adult mucosa, but which also plays a pathological role as the main mode of growth of some intestinal polyps. Building on our previous individual based model for the small intestinal crypt and on *in vitro* cultured intestinal organoids, we here model crypt fission as a budding process based on fluid mechanics at the individual cell level and extrapolated predictions for growth of the intestinal epithelium.

Budding was always observed in regions of organoids with abundant Paneth cells. Our data support a model in which buds are biomechanically initiated by single stem cells surrounded by Paneth cells which exhibit greater resistance to viscoelastic deformation, a hypothesis supported by atomic force measurements of single cells. Time intervals between consecutive budding events, as simulated by the model and observed *in vitro,* were 2.84 and 2.62 days, respectively. Predicted cell dynamics was unaffected within the original crypt which retained its full capability of providing cells to the epithelium throughout fission. Mitotic pressure in simulated primary crypts forced upward migration of buds, which simultaneously grew into new protruding crypts at a rate equal to 1.03 $days^{-1}$ in simulations and 0.99 $days^{-1}$ in cultured organoids. Simulated crypts reached their final size in 4.6 days, and required 6.2 days to migrate to the top of the primary crypt. The growth of the secondary crypt is independent of its migration along the original crypt. Assuming unrestricted crypt fission and multiple budding events, a maximal growth rate of the intestinal epithelium of 0.10 $days^{-1}$ is predicted and thus approximately 22 days are required for a 10-fold increase of polyp size. These predictions are in agreement with the time reported to develop macroscopic adenomas in mice after loss of *Apc* in intestinal stem cells.

Introduction

The process of crypt fission, in which two functional crypts develop from one single crypt, is a rare phenomenon in the healthy small intestinal or colorectal mucosa of adults, but is essential for maintaining and recovering epithelial homeostasis following severe chemical-induced crypt injury [1], cytotoxic chemotherapy [2], or irradiation [3]. Crypt fission is also responsible for increasing the number of crypts required for postnatal development of the intestine [4, 5], and for the sustained expansion of the mucosal surface area following intestinal resection [6]. Thus, this phenomenon regulates mucosal morphology in the large intestine, and the balance between population size of crypts and villi in the small intestine [7]. It has also been reported that crypt fission is instrumental in the growth of epithelial tumours and in particular, in the growth of adenomatous polyps bearing mutations of the adenomatous polyposis coli (APC) gene [8, 9], colorectal adenomas and hyperplastic polyps [10-12] and in small bowel polyposis syndromes including familial adenomatous and hamartomatous syndromes such as juvenile polyposis[13, 14].

The mechanisms regulating the rate of crypt fission remain unclear. A crypt cycle has been postulated in which a small alteration in the balance between cell loss and cell proliferation results in a slow process of crypt enlargement and a gradual compression of cells located in the lower part of the crypt, which is relieved by the buckling of the cell layer out of the crypt base which initiates the fission event [15]. Stochastic models have been applied to explore the stability and asymptotic behaviour of the crypt cycle [16]. In the human colon, calculations indicate a crypt cycle time of between 17 and 30 years [12], while in the mouse the length of the crypt cycle is 0.3-3.6 years [15, 17]. A simple model postulates that the threshold for triggering crypt fission is the doubling of the stem cell number [18]. Several biomechanical approaches, based on the behaviour of solids, have been developed to model buckling configurations in the intestinal epithelium as the result of the growth of the tissue and the elastic properties of the epithelium and/or underlying stroma [19-23].

The main limitation to exploring crypt fission is its low frequency in the healthy mucosa combined with the difficulty of following the fission process in real time. Crypt fission is however frequently observed in cultures of intestinal organoids [24-26]. Crypts growing *in vitro* are rapidly sealed, forming a cyst containing a lumen filled with apoptotic cells. The surface of the cyst undergoes continuous budding events that

grow into crypts, which after protruding from the cyst, undergo fission. Paneth cells present at the base of the crypts and at budding sites [25] provide a crucial niche for $Lgr5^+$ stem cells by secreting Wingless/Int (Wnt) ligands [27]. Crypts deficient in Paneth cells require exogenous Wnt molecules in order to grow *ex vivo*, while factors compensating for the absence of Paneth cell-derived Wnt signals prevent stem cell exhaustion *in vivo* [28]. Buske et al [23] modelled the biomechanics of the formation of buds in the initial cyst, describing the surface of the continuously expanding cyst as an epithelial cell layer provided with a flexible basal membrane whose mechanical properties generate spontaneous proliferation-induced curvatures in the shape of the epithelium. These spontaneous curvatures lead to buckling configurations by inducing the specification into Paneth cells, which in a positive feedback fashion induce a more pronounced curvature of the epithelium, leading to the formation of the bud on the surface of the cyst [23]. The authors identified a set of conditions that lead to the formation of buds in a cyst in continuous expansion, but not for budding and fission in non-expanding crypts.

The purpose of our study was to advance our understanding of crypt fission by integrating biomechanical and cell-based computational models with measurements from fission events in *in vitro* cultured intestinal organoids. Based on empirical observations, we have extended the computational model previously developed for the crypt [29] by adopting an approach based on fluid mechanics that describes the displacement of cell material out of the crypt plane to form buds that grow into crypts. Our findings challenge the traditional belief that crypt fission is a process of crypt base enlargement followed by buckling, proposing instead that bud initiation is generated by the difference in the biomechanical behaviour of neighbouring Paneth and stem cells. The model hypothesizes that the new crypt develops without affecting cell dynamics within the original crypt. Under these conditions, the ability of the original crypt to supply cells to neighbouring villi is not altered throughout the fission process. Ultimately the model has been applied to predict maximal growth of the epithelium by unrestricted crypt fission.

Results

Biomechanical modelling of bud formation

In mouse intestinal organoid cultures, bud formation takes place initially in regions of the primary cyst with high Paneth cell density; initial buds grow into crypts which contain Paneth and stem cells intermingling at their bases (Figure 1). The new crypts undergo budding events that resemble the reported *in vivo* crypt fission phenomena. Figure 2 shows that in organoids crypt fission is a budding phenomenon that starts in regions of high Paneth cell density at the base of the crypts. The mechanism underlying the association of bud formation and Paneth cells is unknown. To circumvent this lack of knowledge, we have postulated that crypt fission is initiated as a budding process by stem cells surrounded by Paneth cells or their progenitors as a result of biomechanical forces.

The computational model previously developed for the crypt [29] describes the configuration of the crypt as a spiral in the crypt base and a helix forming a stack of circular rings. As described in the Methods section we have extended this approach by assuming that the crypt comprises viscoelastic epithelial cells adjacent to each other, and able to deform if a threshold force, which varies depending on the type of cell, is exceeded. Cell growth, division and migration affect the balance between the space required by cell material and the available space in the crypt wall, generating forces that act upon the cells. In response to these forces individual cells flow deforming the shape of the crypt wall and leading eventually to budding initiation. We assume that the proliferative condition of stem cells makes them deformable when subjected to forces generated by changes in their size during growth and division and/or in the available space in the crypt wall. For Paneth cells, deformation occurs when a critical force threshold is exceeded. In order to support this hypothesis, Atomic Force Microscopy (AFM) has been used to measure the Young's modulus of Lgr5-eGFP positive cells and Lgr5-eGFP negative large granular crypt cells. The Young's modulus is a measure of stiffness that quantifies the linear stress-strain relationship in the range of stress where Hook's law holds. Figure 3A shows that the Young's modulus of all but one of the Lgr5-eGFP positive cells was significantly smaller than that of large granular cells by more than 3 times the standard deviation. Lgr5-eGFP positive cells, which were assumed to be stem cells, required significantly smaller

forces to undergo deformation than large granular cells, which were assumed to be Paneth cells. Moreover, we have assumed that cells behave as viscous materials rather than the solid material behaviour described in previous models. Viscoelastic behaviour of cells was demonstrated in force curves. AFM measurements showed the typical separation, or hysteresis, between the approach and retract force curves resulting from viscous behaviour in all assessed cells (Figure 3B).

In order to parameterize our model, we have analysed the results in crypts simulated with several values for the shear stress threshold required for Paneth cells deformation.

Figure 4A compares the time intervals between successive budding events observed *in vitro* with those simulated using several values for the parameter α. This parameter governs the force threshold required for Paneth cell deformation. When α=0, Paneth cells have identical mechanical properties to stem cells. When α=1, the force required to deform Paneth cells is equal to the force generated by a disequilibrium between available and required space equal to one average cell size; if α is smaller or greater than 1, Paneth cell deformation requires forces smaller or greater, respectively, than that generated by one extra cell. When crypts were simulated with α=0 and α=0.1, Paneth cells were deformed with changes in cell size translated in the flow of cell contents from crypt bottom to top without deformations of the crypt wall. This unimpeded flow was due to the non-stress boundary at the top of the crypt because of unrestrictive cell removal. As the value of α increased, Paneth cells became more resistant to deformation so that the increase in size and/or decrease of available space during the cell cycle was not accommodated by the non-deformable neighbouring Paneth cells, leading to protrusion of cell material out of the crypt wall and bud formation. In simulated crypts, the frequency of budding increased rapidly as the value of α increased from 0 to 1 (Figure 4B). The best agreement between simulated and observed distributions of frequencies for the time interval between successive budding events was observed for values of α slightly greater than 1. For instance, the smallest difference between the simulated and observed distribution was detected for α=1.3 (Figure 4B). The median time interval between consecutive budding events observed *in vitro* and simulated with α=1.3 was 2.62 and 2.84 days, respectively. These medians were not significantly different ($p > 0.05$). Moreover, under these assumptions bud formation was associated with single stem cells surrounded by Paneth cells. Figure 4C shows that the probability of budding of one

stem cell surrounded by Paneth cells increases as the resistance to deformation of Paneth cells increases, reaching values of 0.95 for $\alpha > 1$, while the probability of budding for stem cells clusters with 2, 3 or 4 stem cells is very low (ca 0.04) and practically not affected by the resistance of Paneth cells to deformation (Figure 4C).

In our original computational model [29], the ratio of Paneth to stem cells is 3:2 and they intermingle at the base of the crypt due to Notch signalling-driven differentiation. In the crypt base, stem cell descendants differentiate into Paneth cell progenitors or remain as pluripotent stem cells according to Notch signalling, which is activated and inhibits the secretory cell fate if more than 50% of cells in contact belong to the secretory lineage. In addition, cells in the crypt bottom are dynamically relocated to adjust for cell growth and division. These events determine the configuration of the crypt bottom. Figure 4D shows the relative frequency of stem cells clusters with 1 (0.18 relative frequency), 2 (0.32), 3 (0.28) or 4 (0.22) stem cells in simulated crypts, and how these frequencies were similar for all simulations and not affected by the resistance of Paneth cells to deformation or values of parameter α. Figures 4 E-H show an upper view of the displacement of the cell centres on a ring of the crypt during cell deformation under selected mechanical scenarios. When all cells are stem cells (Figure 4E), or intermingling Paneth and stem cells are deformable with the same mechanical behaviour (α=0, Figure 4F) deformations of the ring are not detected. When Paneth cells are more resistant to deformation than stem cells, for instance for α=1.3, changes in the available space due to stem cells growth are not accommodated and lead to protrusion of cell material out of the crypt wall (Figures 4G-H). We assume irreversible cell deformation if more than half of the cell material is protruding out of the plane of the crypt. Irreversible deformations are observed in areas where 1 stem cell is surrounded by Paneth cells alone (Figures 4G-H). In general, irreversible deformations were not detected when 2 or more stem cells are adjacent to each other because the threshold force for the viscoelastic behaviour of Paneth cells is reached before the irreversible protrusion of cell contents (Figure 4H). If the deformation is reversible, at division time, daughter cells locate out of the plane of the crypt. Those stem cell descendants located outside the crypt plane together with the surrounding Paneth cells, form an initial bud protruding from the original crypt that will grow into a new crypt. We have observed *in vitro* that Paneth cells from the original crypt appear to be incorporated into the new crypt (Figure 1) and it has been

demonstrated *in vivo* that crypts newly generated by fission contain numerous Paneth cells from the original crypts [30].

We have assumed a fixed value for the limiting protruding cell material of irreversible deformations. Changing the protrusion threshold for budding would modify the probability of budding of stem cell clusters with different sizes. Should new experimental evidence in support of this mechanism be forthcoming, simulations could be run to fit jointly the parameters governing the force threshold for Paneth cell deformation and the protrusion threshold for bud initiation.

Cell dynamics within crypts during fission

Cell proliferation and differentiation takes place in the secondary crypt according to the hypotheses of the previously developed model [29]. We assumed that mitotic pressure in the primary crypt forces the upward migration of the secondary crypt, which simultaneously grows and protrudes out of the primary crypt. The supplementary Video S1 shows a simulation of a crypt fission event and Figure 5A shows good agreement between the specific growth rates of the new crypt observed experimentally (0.99 $days^{-1}$) and in the simulations (1.03 $days^{-1}$) (Figure 5A). The median values were not significantly different ($p > 0.05$). The good agreement between the growth rates of the secondary crypt in simulated and in observed fission events indicates that the elongation of the secondary crypt is likely based on cell proliferation, which takes place at the same rate as in the primary crypt.

In simulated fission events the upward migration of the secondary crypt along the original crypt has two periods. The first has a very slow migration rate, with the new crypt located at the base of the original crypt, with a second period of rapid upward migration along the primary crypt (Figure 5B). The duration of the first period of very slow migration is highly variable and lasts until the new crypt reaches positions above row 5 in the original crypt, which requires 4 ± 3.3 days. Thus, during the first period some new crypts may fully develop at the base of the original crypt without migrating upwards. This event, predicted by the model, is observed in cultured organoids such as that captured in Figure 6 showing a fully developed crypt at the base of the primary crypt and how this new crypt replaces the original crypt.

Once the secondary crypt reaches positions above the base of the original crypt, it rapidly migrates upwards to the top of the original crypt, which takes on average 1.7 ± 0.72 days. Our model therefore predicts that the bud is confined to the lower portion

of the crypt for approximately 70% of the duration of the fission process. In agreement with this prediction, between 70 to 90% of the observed fission events have been reported to be detected in the lower 1/4 of the crypts in infant rats [7]. In a study of acid injury, most fission events were observed in the lower 2/3 of the crypt [1].

The predicted increase in migration velocity after reaching positions above the crypt base is in agreement with the observed dependency of the migration velocity along the crypt on mitotic pressure, which is greater at higher positions in the crypt [31]. Forces derived from cell growth and division in the primary crypt are sufficient to explain the upward migration of the secondary crypt along the primary crypt, as seen in the close agreement between simulated and observed migration rates (Figure 5A). The Supplementary Video S2 shows a simulation of a crypt undergoing fission and an *in vitro* fission event in an organoid during 1.3 days of the period of rapid migration of the secondary crypt.

In our model, growth and migration of the secondary crypt are independent of each other while cell proliferation and migration within the original crypt are not affected during fission. This has important implications for the functionality of the original crypt, which supplies cells to the *villi* at full capacity throughout the fission process. Figure 7 shows the analysis of the simulation results regarding growth and migration of the secondary crypt. The median time required for the new crypt to reach its final size was 4.6 days (Figure 7A) while the median time to reach the top of the primary crypt was 6.2 days (Figure 7B). These timings agree with the results of a morphological study of the epithelium regeneration after acid injury [1] in which crypt fission was observed 7 days after the injury and the normal appearance of the mucosa was recovered by 14 days post-injury.

Approximately 30% of the simulated crypts reached their final size before reaching positions above row 5 on the primary crypt (Figure 7C). From these crypts, the 5% located at row 0 of the original crypt have a small probability of migrating upwards and could eventually replace the original crypt as observed *in vitro* (Figure 6). Some of the remaining 25% of crypts located at the bottom of the primary crypt could ascend along the original crypt, generating lateral branches and resembling the reported asymmetrical fission events commencing on the lateral crypt walls instead of at the crypt base[8, 10]. Only 3% of the new crypts reach the top of the primary crypt with a small size, equivalent to 10% of the final size of the crypt (Figure 7D). About

75% of the new crypts reach their final size before reaching the top of the primary crypt or the lumen (Figure 7D).

Cell composition in crypts during fission

During expansion of the new crypt, stem cell descendants generated at the crypt base under high Wnt signalling give rise to stem cells and Paneth-secretory cells, while the progeny of stem cells above the crypt base under low Wnt signalling will specify into proliferative absorptive progenitors and secretory-goblet, enteroendocrine and Tuft cells. Deciding between the two fates of secretory and stem/absorptive cells depends on Notch signalling. Our model hypothesis for the crypt is that Notch signalling inhibits secretory fate if more than 50% of the cells they are in contact with belong to the secretory lineage [29]. We have assumed that mature enterocytes are not generated in the new crypt during its expansion.

Figure 8 shows that the simulated average proportions for each cell type in the crypt remain fairly constant during fission. Around the third day after fission commences, the model predicts a slight increase in the proportion of Paneth and stem cells (Figure 8A). Acute activation of β-catenin has been reported to result in frequent budding events at the bottom of colonic crypts *in vivo* accompanied by an increase of the stem cell compartment[32]. Our model predicts that this increase is coincidental with the formation of the bud or stem cell niche for the new crypt but it is rapidly averaged out by the growth of the bud into a new crypt containing all cell types. Thus, the predicted size of the proliferative compartment during fission is on average unaffected (Figure 8B). The deletion of the adenomatous polyposis coli (*Apc*) gene in intestinal stem cells of mice leads to an aggressive expansion of adenomatous polyps by crypt fission. However the proportion of $Lgr5^{+}$ stem cells in tumors remained unchanged with respect to healthy crypts [9]. Similarly, the number of mitotic cells and the size of the cell proliferation compartment in human familial adenomatous polyposis (FAP) crypts or in mouse multiple intestinal neoplasia (MIN) crypts did not differ from that of healthy crypts [8].

Predicting growth of the intestinal epithelium by unrestricted crypt fission

The growth of the intestinal epithelium by crypt fission was predicted based upon the assumption that budding and fission always take place in crypts when a stem cell is surrounded by Paneth cells. Therefore, crypts undergo more than one budding

process simultaneously with budding taking place in the new crypts generated by fission. These assumptions are based on *in vivo* observation of multiple buds arising from the same crypt as reported after injury [3].

Figure 9 shows that the predicted value for the specific growth rate of the intestinal epithelium by crypt fission is approximately 0.10 $days^{-1}$. Thus, about 15.3 and 21.9 days are required to observe a 5 and 10-fold increase in size, respectively. The predicted growth of the epithelium by unrestricted crypt fission agrees with *in vivo* observations in mice after inducing the loss of the *Apc* gene in intestinal stem cells [9]. After *Apc* loss, crypt branches were continuously formed resulting in macroscopic epithelial formations 2-3 weeks post-induction [9]. However, the constant specific growth rate observed *in vitro* and estimated for adenoma formation in Apc^{-} mice seems to differ from the growth kinetics reported for human colonic adenomas. These included relatively mitotically old populations of monoclonal crypts with occasional newly generated subclones, indicating that colorectal tumourigenesis may be characterized by relative stasis with occasional rapid growth of sub-clones [33].

The predicted percentage of crypts undergoing fission in the epithelium was ~37.6% (Figure 9) comparable with prior*in vivo* studies reporting values of 35% and 22% in mice [34, 35], and 18% in humans at fission peaks seen during intestinal development in infants [36]. The percentage of crypt fission events observed in the proximal small bowel of MIN mice varied from 5% to 22% [8].

Discussion

Our individual cell-based approach to modelling the initiation of budding in the intestinal crypt is based on fluid mechanics with cells having heterogeneous viscoelastic properties depending on their lineage. Our model challenges the traditional belief that crypt fission is a process of crypt base enlargement followed by buckling. We propose the formation of a bud that progressively grows into a crypt, migrating upwards along the primary crypt without affecting cell proliferation and migration within the primary crypt, and without compromising the primary crypt capability of providing cells to the epithelium.

Deformations are caused by the forced displacement of cell contents out of the crypt plane forming a bud containing the stem cell niche that will grow into a new crypt protruding from the primary crypt. Simulations under the hypothesis that Paneth

cells are more resistant to deformation than stem cells resulted in budding in regions of stem cells surrounded by Paneth cells, as observed in crypt organoid cultures. In our model, the location of buds depends on the local cell composition determined by Wnt- and Notch-driven cell differentiation, proliferation and migration within the crypt. Crypts with few Paneth cells are unlikely to undergo fission events, while an increase in the ratio of Paneth cells to stem cells increases the predicted frequency of budding. The model hypothesis could be generalized for the whole crypt by assuming that proliferative absorptive progenitors behave mechanically as stem cells while secretory cells have the same deformation threshold as Paneth cells. Budding takes place only when proliferative cells are surrounded exclusively by secretory cells. In normal conditions, this configuration would only be observed in the stem cell niche at the base of the crypt.

The mechanisms responsible for the initiation of buds in the intestinal crypt, both *in vivo* and *in vitro*, are as yet unknown. Although the hypothesis underlying bud initiation in our fluid mechanics approach lacks experimental evidence, the good agreement between the observed budding frequency *in vitro* and the frequency predicted by our biomechanical approach for the normal ratio between Paneth and stem cells in the crypt validates its use to predict epithelial growth by crypt fission.

Biomechanical approaches are commonly applied to modelling the buckling of a growing epithelium. The analysis of the patterns created by buckling of a dividing epithelial monolayer of cells lying on top of an elastic stroma results in a variety of possible conformations of crypts and villi along the small intestinal epithelium [21, 37]. Modelling a growing epithelium attached to a basement membrane has also been demonstrated to be useful to study interactions between epithelium and stroma in the crypt [38]. This kind of biomechanical approach has been applied specifically to model crypt fission [19, 20, 22, 39]. These models consider the epithelium as a solid beam formed by adjacent cells subjected to stretching and compression forces generated by an increase in the number of cells, leading to buckled conformations. The cell-based approach of Drasdo [19] and Drasdo and Loeffler [39] describes the bending of the epithelium in a two dimensional system and identifies cell proliferation as the main reason for the onset of buckling. In the continuous approach modeling of Edwards and Chapman [20], the epithelium is modeled as a growing beam attached to an underlying lamina in 2 dimensions. In this model, the buckling of the tissue is in response to any combination of an increase in cell proliferation, an enlargement of the proliferative

compartment and/or an increase in the strength of cellular attachment to the underlying lamina. A further analysis of this approach shows that non-uniform growth patterns along the epithelium have a much weaker influence on the buckled shapes than non-uniformities in the mechanical properties of the material [22]. The same authors have recently claimed that in a three-dimensional system, growth patterning has a greater impact on the distribution of crypts than does material inhomogeneity[37]. A distinctive feature of our approach to modelling crypt fission is that we treat cells as viscous materials rather than assuming the solid material behaviour described in the models discussed above. In agreement with *in vitro* experimental observations, we have modelled fission as a budding process based on fluid mechanics at the individual cell level and not, as the folding or buckling of solid material. AFM measurements confirmed the viscous nature of both LGR5-eGFP positive and LGR5-eGFP negative large and granular single cells isolated from crypts (Figure 3B). Moreover, we modelled fission as a consequence of inequalities in the mechanical properties of viscoelastic cells which depend on cell lineage. This hypothesis was also supported experimentally by AFM measurements of single cells, which revealed that stem cells are less stiff than other granular large crypt cells.

Another distinctive feature of our model is that, changes in the size of the proliferative compartment or in the division rate are not associated with budding. Although fission ultimately depends on cell division, there is uncertainty regarding the relationship between changes in cell proliferation and crypt fission. The increase in cell proliferation within the crypt, or in crypt volume, has been reported in several studies not to be associated with crypt fission[10, 40-42]. Indeed, the administration of epithelial growth factor to MIN mice resulted in an increased cell proliferation within crypts with a significant reduction in the rate of fission [41]. Similarly, studies on intestinal development in infant rats and humans concluded that crypt fission is not always preceded by crypt hyperplasia[36, 42]. Also, the administration of P-cadherin results in enhancement of crypt fission *in vivo* while cell proliferation in crypts is unaffected [43]. Similarly, in MIN mice the proportion of crypts in fission increases dramatically but cell proliferation is not affected in dividing crypts compared to stable crypts [8]. In another study, a reduction in intestinal crypt fission was detected after the administration of the negative regulator of Wnt signalling, dickkopf, although cell proliferation remained unchanged [44].

Apc loss induces acute activation of Wnt/β-catenin signalling pathway. The activation of the Wnt pathway induces *de novo* specification of Paneth cells in the mouse small intestine. Both murine colon polyps and human colonic tumours resulting from *Apc* mutations express genes involved in Paneth cell differentiation [45]. Although Paneth cells are absent from both mouse and human colon, a subset of colonic secretory cells that share cKit$^+$ expression with small intestinal Paneth cells, and are essential for the maintenance of the stem cell niche and for organoid formation *in vitro*, have been identified in the base of colonic crypts intermingled with Lgr5$^+$ cells [46].

In the small intestine, the relationship between Paneth cells and the two pools of intestinal stem cells, slow cycling cells located at position +4 and actively cycling stem cells at the bottom of crypt, is not well understood. It has been demonstrated that Paneth progenitor cells revert to stem cells upon crypt damage [47, 48], and specifically quiescent +4 stem cells have been identified with secretory progenitors expressing Lgr5 and able to regain 'stemness' after intestinal injury [49, 50]. In mouse colonic crypts Wnt activation has been demonstrated to induce crypt fission, accompanied by a reduction in the cell proliferation rate and of activation of the Notch signalling pathway among progenitors [32]. Therefore under Wnt activation, crypt fission could be associated with enhancement of the slowly cycling secretory progenitors, which is in agreement with the increase of budding linked to the increase in the ratio of secretory cells to stem cells predicted by our model.

We have observed buds in regions with Paneth cells although we have not experimentally determined the density of Paneth cells in budding regions. It has been reported that numerous Paneth cells from the primary crypt are detected in newly generated crypts by fission *in vivo* [30]. In this published study, crypt fission is assumed, though not experimentally proven, to be a progressive longitudinal partition initiated at the crypt base. However, if fission is a budding process as we propose here, the abundance of original Paneth cells in the base of the new crypt indicates that Paneth cells or their progenitors are present in high numbers in the region where the bud is initiated and they form part of the initial bud. On the other hand, an essential role of Lgr5$^+$ stem cells in crypt fission in the intestine [30] and also in gland fission in the stomach [51] has been demonstrated using *in vivo* clonal fate mapping strategies to observe the lateral expansion of Lgr5-expressing stem cell derived clones, containing clonal Lgr5$^+$ stem cells.

It should be noted however that ablation of Paneth cells does not affect deregulation of crypt fission and intestinal tumourgenesis in *Apc* mice with intestinal stem cells deficiency [28]. Non-canonical Wnt signalling has also been associated with crypt regeneration in the wounded epithelium of mice [52]. Wnt5a molecules, which are non-canonical Wnt ligands that inhibit intestinal cell proliferation *in vitro*, have been detected in stromal mucosal cells localized to clefts in-between nascent crypts *in vivo*, seemingly contributing to defining the shape of the new crypts in injured areas of the epithelium where crypts have been excised [52]. A common denominator seen in circumstances preceding non-tumour growth-associated crypt fission *in vivo* is a diminished density of functional healthy crypts in the mucosa. For example, as seen during intestinal growth in infants [35, 36], compensatory intestinal dilation following intestinal resection [6], and during recovery of wounded areas of the mucosa [1, 52]. The role of Wnt signalling and Paneth cells in the regulation of crypt fission *in vivo* is therefore complex and other components, potentially of mesenchymal origin, are likely to be involved.

In our simulated crypts, unrestricted crypt fission is associated with a biomechanical instability generated by difference in the biomechanical properties of Paneth and stem cells. We can hypothesize that the progression of the instability to form an initial bud is inhibited *in vivo,* while the inhibitory mechanism is absent in the *in vitro* culturing system. This hypothesis was developed to circumvent the lack of information regarding the signalling and regulation of the fission process. Although under this hypothesis the predicted and observed budding frequencies are in good agreement (Figure 4A), further experimental validation is required. In addition, the cellular Wnt and Notch signalling pathways function normally in both the simulated crypts and in the *in vitro* cultured crypts. However, Apc^{-} mice have a severely altered Wnt signalling pathway. Therefore, although the rates of fission appear to be similar, the mechanisms behind unrestricted crypt fission *in vivo* and *in vitro* are likely to be very different. One of the essential factors required to maintain intestinal stem cells and organoids in culture is R-spondin [53]. This protein strongly potentiates the Wnt signalling pathway and, just as in the case of the deletion of the Wnt signalling inhibitor APC *in vivo* [8, 12, 54], this may account for the unimpeded epithelial growth by crypt fission observed *in vitro*. Thus, crypts cultured *in vitro* under acute stimulation of the Wnt signalling pathway, and *in vivo* crypts with a disinhibited Wnt target gene

480 programme, may achieve maximum crypt fission rates, which would explain the
481 similarity of the epithelium growth kinetics in these two different systems.
482 In summary, the model we have presented shows how crypt budding can be
483 biomechanically initiated by stem cells surrounded by Paneth cells which accurately
484 predicts epithelial growth by unrestricted crypt fission as observed in cultured
485 organoids. The epithelial growth rate predicted by unrestricted crypt fission agrees
486 with the growth observed *in vivo* in intestinal adenomas associated with APC loss. We
487 have therefore integrated individual based models with *in vitro* culturing organoids to
488 develop an approach able to simulate the process of crypt fission and further
489 extrapolated predictions for the growth of adenomatous polyps in the mouse intestinal
490 epithelium. The generated modelling framework can be applied to test hypotheses on
491 regulation mechanisms in homeostatic crypts and to explore the impact of
492 perturbations on the progression of adenoma-carcinoma processes in the intestine.

Methods

Animal care and experimentation were performed in accordance with the Guidelines established by the Committee on Animal Care and Use of Keio University and under the authority of the UK Home Office (PPL 80/2355).

Preparation of *in vitro* crypt cultures

Small intestinal crypt preparations from 6 week old mice (strain C57/B6 or Lgr5-EGFP-ires-CreERT2) were embedded in Matrigel (BDBioscience). After polymerization of Matrigel, crypt culture medium (advanced DMEM/F12 supplemented with Penicillin/Streptomycin, 10 mM HEPES, Glutamax, 1x N2, 1x B27 [Invitrogen], and 1 µM N-acetylcysteine [Sigma] and containing 50 ng/ml EGF [Peprotech], 100 ng/ml noggin [Peprotech], 1 µg/ml R-spondin 1) was overlaid. Cultures were maintained as previously described [53].

The growth of organoids was imaged using a climate-controlled (37°C, 5% CO2) stage of an inverted motorised time-lapse microscopic system (Nikon) for periods of up to 10 days. Frames of ten movies including 1-3 organoids each were analysed to estimate budding frequency per crypt, the growth of the secondary crypt and its migration along the original crypt.

Fluorescent immunostaining and confocal microscopy

Organoids were isolated from Matrigel using Cell Recovery solution (BD Biosciences) and fixed with 4% paraformaldehyde (PFA). After fixation, samples were incubated with 0.2% Triton X-100 in PBS for permeabilization, and with Universal Blocking Reagent (Biogenex) for blocking non-specific binding of antibodies. To visualize Lgr5+ stem cells and lysozyme+ Paneth cells, samples were incubated overnight at 4℃ with antibodies specific for GFP (abcam; ab6673, 1:100) and Lysozyme (Dako; A0099, 1:1000) in PBS. GFP and Lysozyme were labelled by anti-Goat alexa488 conjugated antibody and anti-Rabbit alexa568 conjugated antibody (Invitrogen) in PBS. Nucleus was counterstained with Hoechst33342. Images were acquired by confocal microscopy (Leica SP8).

Crypt and epithelial cell isolation

Crypts were isolated from whole small intestine of C57BL/6-J or Lgr5-eGFP$^{tm1(cre/ERT2)Cle/J}$ adult mice at 12-16 weeks of age. Whole intestines were flushed,

and dissected in PBS containing antibiotics and antimycotics. Samples were incubated on ice in 2 x 5 mins 1mM DTT and 3 x 5 mins 2mM EDTA, with gentle shaking to remove debris and sloughed epithelial cells. Remaining epithelial cells and crypts were dislodged by 30 min incubation in 2mM EDTA at room temperature, then vigorously shaken in successive fractions of ice-cold PBS. Crypts were spun down, concentrated and incubated 35 min at 37°C with collagenase/dispase (Roche) and DNase I (NEB) to generate a single-cell suspension. GFP-positive (Lgr5-eGFP stem cells) and GFP-negative cells (non-stem epithelial cells) were separated using a Sony SH-800 cell sorter. Cells were re-suspended in advanced DMEM containing B27, N2, n-acetylcysteine (1 mM), HEPES (10 mM) penicillin/streptomycin (100 U/ml), L-Glutamine (2 mM), epidermal growth factor (50 ng/ml), Wnt-3A (100 ng/ml), Noggin (100 ng/ml) SB202190 (20 μM), seeded onto poly-lysine coated slides and allowed to adhere overnight at 37°C / 5% CO_2. Media was replaced with D-PBS with Ca^{2+}/Mg^{2+}, immediately prior to measurement by atomic force microscopy.

Atomic Force Microscopy AFM

The AFM used for this study was an MFP-3D-BIO (Asylum Research, Santa Barbara, CA. USA). The deformability measurements were performed with a cantilever fitted with 2.5 μm diameter silica bead in place of the AFM tip (CP-PNPL-SIO-A, sQUBE Surface Science Support, Germany). This is necessary for two reasons; firstly to prevent penetration of the cell membrane by the AFM tip during the measurements, and secondly to allow proper quantification of the indenter shape for subsequent modelling [55].

Prior to the cell deformation measurements, the optical lever sensitivity of the cantilevers was calibrated by pressing against a rigid surface (clean glass slide) The spring constants of the cantilevers were determined using the thermal noise spectra method [56].The AFM sits on top of an inverted optical microscope (IX-71, Olympus, Japan) enabling the AFM tip to be accurately positioned on chosen cells. The optical microscope was operated in epi-fluorescence mode to enable discrimination of the Lgr5-eGFP+ stem cells. Deformability of the cells was measured by performing multiple force versus distance curves at a velocity of 2 $\mu m.s^{-1}$ on the chosen cells. Two controlled maximum load forces (600 pN and 1.2 nN) were applied to ensure sufficient, but not excessive, deformation was achieved. The data was fitted to a

559 Hertzian elastic model featured in the instrument software which analyses it in terms
560 of force versus indentation (MFP-3D 111111+1610).
561
562 **Biomechanical model for the initiation of buds**
563 Cells are modelled as spherical shapes of incompressible homogenous viscous
564 material which are packed to form the walls of the crypt. Cells maintain their shape in
565 the absence of stress, but under an applied sufficient stress, cell material flows and
566 changes cell shape, accumulating stress in return. When the accumulated stress and
567 the applied stress have the same magnitude, the cell material is no longer displaced.
568 When the applied stress is removed, cells could partially return to their original form
569 (viscoelastic behaviour) or maintain some degree of deformation (viscoplastic
570 behaviour); constant cell proliferation generates a certain compression force in the
571 system that prevents the absolute relaxation of the system.
572 We describe the crypt as a cylindrical structure organized in 3 dimensions with
573 rings of cells in the XY horizontal plane and a vertical axis, Z, from the base to the
574 top of the crypt (Figure 10). Proliferative cells, which include stem cells, are assumed
575 to behave as Newtonian fluids under forces derived from cell growth; however mature
576 cells including Paneth cells, behave as Bingham plastics. With these assumptions, the
577 viscoelastic behaviour of stem cells is defined by one parameter, the dynamic
578 viscosity coefficient, μ, derived from the linear relationship between the shear force,
579 τ, and the shear rate, $\partial v/\partial x$. For laminar flows this can be expressed as: $\tau = \mu(\partial v/\partial x)$
580 where v is the velocity and x the orthogonal dimension to the direction of the flow.
581 The behaviour of Paneth cells is described by two parameters, the apparent viscosity
582 coefficient, η, and the shear stress threshold or yield point, τ_T, i.e. $\tau = \tau_T + \eta(\partial v/\partial x)$.
583 Paneth cells exhibit linear shear stress, shear rate behaviour only after the shear stress
584 threshold, τ_T, has been reached. Hence, to deform Paneth cells, the driving shear stress
585 has to be larger than τ_T, and because of this threshold, Paneth cell deformation differs
586 from stem cell deformation. The shear rate or velocity gradient, $\partial v/\partial x$, of Newtonian
587 fluids decreases gradually towards the cell centre and reaches a value of 0 at the axis
588 of symmetry or $x = 0$ giving place to a gradual deformation of the shape of the edge
589 (Figure 10). Bingham plastics behave as solids when the force is below the shear
590 stress threshold which results in the formation of a solid plug at the front of the

deformed edge of the cell moving with the flow (Figure 10), i.e $\partial v/\partial x=0$ at $x = x_T$, which is the radio of the solid plug.

Assuming zero-stress boundary conditions at the top of the crypt because of the unrestrictive removal of cells, when all cells have the same mechanical properties, cell growth is translated in the flow of cells in the parallel direction to the Z axis within the crypt wall. Flow within the crypt wall in other directions is also possible, but not frequent, due to the fully packed condition of the crypt walls. The other direction that the flow may take is the orthogonal direction to the Z axis, out of the crypt wall (Figure 10).

When Paneth cells behave as Bingham plastics, the flow may be disturbed by the presence of these cells with higher resistance to deformation which are obstacles to the flow of the viscous cells, and eventually they may force the change of the direction of the flow towards the X and Y directions, i.e. deforming the external side of the crypt wall (Figure 10).

The deformation of the external side of the cells occurs when one or more adjacent viscous, i.e. deformable, cells, whose geometric centres form a convex set, are delimited by cells that will exhibit viscous behaviour only after a given threshold force is reached. Flow analysis in three dimensions can be carried out under the assumption of laminar flow. To analyse the deformation of the external side of the cell, it is sufficient to analyse the flow in two dimensions in either the XZ plane or of the XY plane as described in Figure 10. The analysis of the deformation in these two planes is equivalent under the hypothesis of axial symmetric flow (Figure 10). As an example, we describe below the deformation of rings formed by two- dimensional cells in the XY plane (Figure 10). The analysis is exactly the same for a two-dimensional longitudinal section of the crypt.

The Navier-Stokes general equations for an incompressible two-dimensional flow are:

$$\frac{\partial v_y}{\partial t}+v_x\frac{\partial v_y}{\partial x}+v_y\frac{\partial v_y}{\partial y}=-\frac{1}{\rho}\frac{\partial P}{\partial y}+\nu\left(\frac{\partial^2 v_y}{\partial x^2}+\frac{\partial^2 v_y}{\partial y^2}\right) \quad (1)$$

$$\frac{\partial v_x}{\partial t}+v_x\frac{\partial v_x}{\partial x}+v_y\frac{\partial v_x}{\partial y}=-\frac{1}{\rho}\frac{\partial P}{\partial x}+\nu\left(\frac{\partial^2 v_x}{\partial x^2}+\frac{\partial^2 v_x}{\partial y^2}\right) \quad (2)$$

And the continuity condition for incompressible flow,

$$\frac{\partial v_x}{\partial x} + \frac{\partial v_y}{\partial y} = 0 \quad (3)$$

In equations (1) through (3), v_x and v_y are the velocity components of the flow in the x and y direction, respectively, t is time, ρ is density, v is the kinematic viscosity and P is the pressure per unit length, which is uniformly applied to the edges of a two dimensional cell in the direction of the motion of the liquid due to compression (Figure 10). Cell compression is derived from the difference between cell size and available space. We have described the deformation of free external cell sides only. The deformation of free internal cell sides facing the crypt lumen could be similarly analysed. With a perfect laminar flow, the pressure in both internal and external cell sides and therefore cell content displacement in each direction will be proportional to the area of each cell side. Due to the organization of cells in rings the area of the internal cell side is smaller than the area of the external side. For instance, in our crypt, cell protrusion towards the lumen will be in average only 20% of the external cell protrusion. In addition, it is likely that cell structural properties perturb the flow and decrease cell displacement towards the lumen. For these reasons, we have disregarded the analysis of cell protrusion towards the lumen of the crypt.

As described in Figure 10, the laminar flow in two dimensions driven by a constant pressure gradient, $-\partial P / \partial y = K$, takes place essentially in the y direction and hence, $v_x = 0$ which when replaced into equation (3), produces $\partial v_y / \partial y = 0$. These two conditions, $v_x = 0$ and $\partial v_y / \partial y = 0$, simplify equations (1) and (2) to the following:

$$\frac{\partial v_y}{\partial t} = -\frac{1}{\rho}\frac{\partial P}{\partial y} + \nu \frac{\partial^2 v_y}{\partial x^2} \quad (4)$$

$$0 = -\frac{1}{\rho}\frac{\partial P}{\partial x} \quad (5)$$

Equation (5) indicates that P is not a function of x, then $\partial P / \partial y = dP / dy = -K$ which combined with in equation 4 results in the governing equation:

$$\frac{\partial v_y}{\partial t} = \frac{K}{\rho} + \nu \frac{\partial^2 v_y}{\partial x^2} \quad (6)$$

Assuming that the flow is in steady state, i.e. $\partial v_y / \partial t = 0$, equation (6) becomes:

$$\frac{d^2 v_y}{dx^2} = -\frac{K}{\mu} \quad (7)$$

For stem cells behaving as a Newtonian fluid, $\mu = \rho v$ is the dynamic viscosity of the fluid. The x variable describes the distance of the cell content being displace from the cell centre in the XY plane and hence takes values in the interval (-R, R) (Figure 10). With the condition, $dv_y/dx = 0$ at $x = 0$ derived from the axial symmetry assumption, and the no-slip condition at the boundaries, i.e. $v = 0$ at $x = R$, equation 7 has solution:

$$v_y(x) = \frac{dy}{dt} = -\frac{K}{2\mu}(x^2 - R^2) \tag{8}$$

Equation 8 is the Poiseuille law for a two-dimensional fluid and it describes the velocity of cell material located at a distance x from the cell centre in the XY plane

The area of the surface, S, displaced in dt, or flow rate, can be estimated by integrating equation 8 on x from -0 to R and multiplying the result by 2:

$$\frac{dS}{dt} = \frac{2}{3}aR^3 \tag{9}$$

Where $a = \frac{K}{\mu}$

For Paneth cells behaving as Bingham plastics, $\eta = \rho v$ is the apparent viscosity of the fluid and equation 6 is as follows

$$\frac{d^2 v_y}{dx^2} = -\frac{K}{\eta} \tag{10}$$

With the condition, $dv_y/dx = 0$ at $x = X_T$, which is the radio of the symmetric solid plug at the center of the flow (Figure 10) and the no-slip condition at the boundaries, i.e. $v = 0$ at $x = R$ and at $x = -R$, equation 7 has solution:

$$v_y(x) = \frac{dy}{dt} = -\frac{K}{\eta}\frac{(x^2 - R^2)}{2} + \frac{K}{\eta}X_T(x - R) \tag{11}$$

The corresponding flow rate is:

$$\frac{dS}{dt} = 2\left(\int_{X_T}^{R} -\frac{K}{2\eta}(x^2 - R^2) + \frac{K}{\eta}X_T(x - R)dx + X_T v_y(X_T)\right) =$$

$$= b\left(\frac{2}{3}R^3 + \frac{1}{3}X_T^3 - R^2 X_T\right) \tag{12}$$

Where $b = \frac{K}{\eta}$

As the cell material is incompressible, the value dS/dt, can be estimated from the change in cell size and available space as follows:

$$\frac{d\hat{S}}{dt} = \sum_{k \in I} \frac{dA(cell_k)}{dt} - \frac{dA(\text{space available for } I \text{ set})}{dt} \quad (13)$$

where I is the set of adjacent cells forming a convex set with identical viscous behaviour and A the area of surface.

Equation 9 and 12 are identical when the shear stress threshold in Paneth cells is equal to zero and Paneth and stem cells have the same coefficient of viscosity, $\mu = \eta$. Under these conditions, the values of the parameters a and b, can be estimated from equation 9 or 12 and 13, respectively. The assumption of equal coefficient of viscosity for stem and Paneth cells also simplifies the description of the shear stress threshold in Paneth cells as described below.

In order to quantify the formation of buds with different values for the shear stress threshold in Paneth cells, τ_T, and to provide a rough biological interpretation, the relationship between the shear stress and the pressure gradient due to cell growth can be described as

$$\tau(x) = -x\frac{dP}{dy} \quad (14)$$

And the shear stress threshold in Paneth cells can be expressed as:

$$\tau_T = X_T K \quad (15)$$

By substituting in equation 11:

$$v_y(x) = \frac{dy}{dt} = -\frac{K}{2\eta}(x^2 - R^2) + \frac{\tau_T}{\eta}(x - R) \quad (16)$$

From equation 9 for the flow rate in stem cells, an average pressure gradient can be estimated as a function of the average growth rate of the surface area of stem cells, r_{av}, and an average stem cell ratio at birth, R_{av}, as follows:

$$K_{av} = \frac{3}{2}\frac{\mu}{R_{av}^3} r_{av} \quad (17)$$

From equation 14 and 17, the average force exerted by the compression due to one extra cell can be described as follows;

$$\tau_{av} = R_{av} K_{av} = \frac{3}{2}\frac{\eta}{R_{av}^2} r_{av} \quad (18)$$

From equation 18 and under the assumption that $\eta = \mu$, values for the ratio τ_T / η in equation (16) can be chosen to be proportional to the average shear rate in stem cells

$$\frac{\hat{\tau}_T}{\eta} = \alpha \frac{\tau_{av}}{\mu} = \frac{3}{2} \frac{r_{av}}{R_{av}^2}$$

And therefore,

$$\hat{\tau}_T = \alpha \tau_{av} \quad (19)$$

Where α is a factor of proportionally between the shear force threshold required to deform Paneth cells and the compressive forces generated by a disequilibrium between the required and the available space equal to one cell size; α takes values equal to or greater than zero. If α=0, Paneth cells behave as a Newtonian fluid and its deformability is identical to that of stem cells. If α=1, the shear force threshold required to deform Paneth cells is equal to the compressive forces generated by one extra cell; if α is smaller or greater than 1, Paneth cells deformation requires forces smaller or greater, respectively, than those generated by one extra cell. The initiation of budding and fission takes place because of the instability of the cell shape. We assume irreversible cell deformation, if more than half of the cell material is protruding out of the plane of the crypt. Less extreme deformations of the cell are considered reversible. Thus, when the protrusion of cell material is significant, at division time, daughter cells will locate out of the plane of the crypt, initiating a bud that grows into a new crypt.

In order to study how budding depends on the shear force threshold of Paneth cells, the probability of budding within a period of 12 and the time intervals between successive budding events in a single crypt were quantified in simulations run with α values equal to 0.1, 0.3, 0.5, 0.7, 0.8, 0.9, 1, 1.1, 1.2, 1.3, 1.5, 2.

Integration of the bud initiation process in the individual based model for the crypt of Pin et al [29] and analysis of forces.

The model of Pin et al [29] has been adapted to describe crypt fission in a three dimensional crypt. Model parameters are summarized in Supplementary Table S1. In the original model, the structure of the bottom of the crypt is modelled as a three-dimensional spiral followed by the crypt body, which is a three-dimensional helix, constructed from single cells organized in a one-dimensional chain. The position of any cell in the spiral or helix is determined by the coordinates of the cells organized in rings in the XY plane and the vertical coordinate Z, which describes the height reached by cells in columns perpendicular to the XY plane. At each interval time of

the simulation, the three dimensional spiral and helix are re-built according to the change in cell, and division or deletion events. Growing cells expand homogenously in all directions. The increase in cell size in the vertical direction creates a force translated mostly in upward migration. Cell size changes in the horizontal plane are accommodated by changing the perimeter of the ring in the XY plane perpendicular to the crypt-villus axis.

In the new version of the model, growing cells expand in the vertical Z direction, unless the force generated by growth is not enough to deform neighbouring Paneth cells, which in that case are obstacles to the flow that force cell shape deformation in the XY plane protruding out of the crypt wall.

The Monte Carlo simulation previously described [29] has been extended by updating the cell viscous behaviour and accordingly cell position at each time-step. Time-steps include division times. All other cell properties such as size, type, age are updated as previously described [29]. A summary of the extended approach is as follows:

1) Proliferative and stem cells grow, increasing their size to reach twice their original size by division time according to the proliferation rates previously described [29]. Non-proliferative cells also grow at those rates until they reach their final size.

2) The viscous behaviour of non-growing cells, such as mature Paneth cells, and the sets of deformable cells are evaluated by comparing the ratio between the overall size of neighbouring deformable cells and the available space. Paneth cells subjected to forces that are not greater than the threshold and are not deformable and remain in their original position. The deformation out of the crypt plane of growing stem cells surrounded by non-deformable Paneth cells is quantified as described in the section above. When the protrusion of cell material is significant, at division time, the daughter cells will form a bud located out of the plane of the crypt.

3) In regions where all cells are deformable, the increase of cell size takes place within the crypt wall and the cell deforms mainly in the direction of the crypt longitudinal, or Z, axis. At each time step, the crypt is reorganized to accommodate changes in cell size, which are translated in changes in the Z coordinate for the majority of cells, while cell coordinates in the XY plane practically do not change. Dividing cells partition into two daughter cells with similar size which is randomly apportioned [29]. The division event does not imply any increase of cell size, however, in practice, after division the one dimensional chain used to build the three

768 dimensional helix has to be reorganized to assign an index to the new cell as
769 previously described[29]. One of the daughter cells is assigned with the index of the cell
770 located in the ring immediately above. The vertical adjustment of indices spreads
771 upwards along the crypt until the cell in the last ring. The position and shape of the
772 relocated cell are accommodated to fit the space occupied by the cell immediately
773 above and this has an impact on cell displacement. To quantify this impact, we have
774 measured the velocity of cells during time intervals that include index rearrangement
775 and compared it with velocities of cells that do not change the ring. Supplementary
776 Figure S1 shows the comparison of the total distance and the distance in each
777 dimension travelled by cells during time intervals with and without index
778 reassignment. We have estimated that on average index reassignment takes place in
779 the crypt in 20% of the cell movements and it generally causes a small increase of the
780 total travelled distance by the cell by affecting mainly cell displacement on the XY
781 plane (Supplementary Figure S1); this is because cells are not aligned along the crypt
782 wall. Despite the impact of the index reassignment process on cell displacement, our
783 approach is a good approximation to describe continuous cell growth and migration
784 and cellular compaction within the crypt in a similar way to lattice free models [57-60]
785 and therefore, it differs from automota cell models using rigid lattices [61, 62] in which
786 cells migrate by discontinuous large movements.
787 In our approach, cell migration is exactly modelled as the result of the balance
788 of forces during the process of cell deformation out of the crypt plane. However, cell
789 migration within the crypt plane is simulated by a Monte Carlo approach without
790 applying explicit energy balance equations. This is possible because inertial forces are
791 neglected and cell displacement is assumed to be the consequence of cell growth only,
792 that are common assumptions when modelling cell dynamics in the crypt [59, 63]. To
793 evaluate the applicability of our model, we have compared simulated cell velocities
794 with theoretical cell velocities resulting from the total force exerted by neighbouring
795 cells as the consequence of cell growth and migration [63]. Supplementary Figure S2
796 shows that the simulated and theoretical velocity is practically the same for a high
797 percentage (~70%) of cells when they do not change index position in the helix.
798 During cell relocation in the helix, the balance of forces is maintained only in ~40%
799 of the cases while for the rest, the simulated velocity is greater than the theoretical
800 velocity (Supplementary Figure S2). Therefore, a proportion of punctual cell
801 velocities with our modelling approach could be slighted overestimated.

Computational model for the development of a new crypt from the crypt partition process.

The biomechanics of the progression of the initial deformation towards a new crypt is currently unknown and we have therefore adopted a simple descriptive geometrical approach. The initial bud is assumed to be formed by the newly generated cells after division and the surrounding Paneth cells from the original crypt; with practically no displacement of Paneth cells, the initial spiral is located orthogonally to the tangent plane to the original stem cell centre. The new crypt is developed from the bud by proliferation and differentiation of cells that progressively form a new spiral and helix according to a given final number of crypt cells as previously described [29]. The final size of the new crypt is assumed to be equal to the size of the primary crypt.

We assume that cells in the bud proliferate and generate a new crypt, protruding from the primary crypt independently of the primary crypt. In the primary crypt the insertion of the new crypt is represented by a disk of a diameter equal to the secondary crypt mouth. The new crypt is located orthogonally to the tangent plane to the central point of the crypt insertion disk and therefore, the lumens of both crypts are assumed to be connected from the earliest stage (Supplementary Figure S3). Cell differentiation and proliferation in the primary crypt is not affected by the presence of the bud so that the primary crypt deals with the area of insertion of the new crypt in the same way as with no budding regions.

Mitotic pressure in the primary crypt forces the upward migration of the secondary crypt, which simultaneously grows and protrudes out of the primary crypt. Thus, the growth and migration of the secondary crypt are independent processes. We assumed that when the secondary crypt reaches its final size its length stops increasing and cell proliferation forces either cell shedding into the lumen, or cell migration to any adjacent villus structures or to the walls of the primary crypt, whilst the secondary crypt has not yet reached the top of the primary crypt. Crypt fission or partition occurs when the secondary crypt reaches the top of the primary crypt.

Stochastic simulation of the growth of the intestinal epithelium by crypt fission

We developed a Monte-Carlo simulation algorithm to simulate the growth of the intestinal epithelium. The time for the following budding event in a crypt is generated by randomly sampling from the histogram of the time intervals between

836 budding events in Figure 4A; the specific growth rate is assigned to each crypt by
837 randomly sampling from the simulated histogram in Figure 5A. Budding times are
838 used as time steps. At each time step, a new crypt formed by 1 cell is added into the
839 epithelium and the size of all growing crypts is updated. Crypts stop growing after
840 reaching their final size. Simulations were started from a single crypt.
841
842 **Statistical Analysis**
843 Growth rates were estimated by lineal regression after the logarithmic
844 transformation of the dependent variable when required. Median values were
845 compared by a Wilcoxon-Mann-Whitney test**.**
846

847 ## Acknowledgments
848 Authors kindly acknowledge the help of Gary Barker with modelling the
849 behaviour of viscoelastic material.
850

References

1. L. Cheng, K. Araki, Y. Furuya, T. Matsuoka, K. Mashima, M. Kobayashi and K. Matsuura, *Med Electron Microsc*, 2000, 33, 165-171.

2. N. A. Wright and A. Al-Nafussi, *Cell Tissue Kinet*, 1982, 15, 611-621.

3. A. B. Cairnie and B. H. Millen, *Cell Tissue Kinet*, 1975, 8, 189-196.

4. N. A. Wright and M. R. Alison, *The biology of epithelial cell populations. Volume 2*, Clarendon Press, Oxford, 1984.

5. R. M. Clarke, *J Anat*, 1972, 112, 27-33.

6. C. M. Dekaney, J. J. Fong, R. J. Rigby, P. K. Lund, S. J. Henning and M. A. Helmrath, *American journal of physiology. Gastrointestinal and liver physiology*, 2007, 293, G1013-1022.

7. W. H. St Clair and J. W. Osborne, *Cell Tissue Kinet*, 1985, 18, 255-262.

8. H. S. Wasan, H. S. Park, K. C. Liu, N. K. Mandir, A. Winnett, P. Sasieni, W. F. Bodmer, R. A. Goodlad and N. A. Wright, *J Pathol*, 1998, 185, 246-255.

9. N. Barker, R. A. Ridgway, J. H. van Es, M. van de Wetering, H. Begthel, M. van den Born, E. Danenberg, A. R. Clarke, O. J. Sansom and H. Clevers, *Nature*, 2009, 457, 608-611.

10. N. A. Wright, *Int J Exp Pathol*, 2000, 81, 117-143.

11. W. M. Wong, N. Mandir, R. A. Goodlad, B. C. Wong, S. B. Garcia, S. K. Lam and N. A. Wright, *Gut*, 2002, 50, 212-217.

12. A. Humphries and N. A. Wright, *Nat Rev Cancer*, 2008, 8, 415-424.

13. A. P. Haramis, H. Begthel, M. van den Born, J. van Es, S. Jonkheer, G. J. Offerhaus and H. Clevers, *Science*, 2004, 303, 1684-1686.

14. N. Arber and M. Moshkowitz, *Curr Gastroenterol Rep*, 2011, 13, 435-441.

15. J. Totafurno, M. Bjerknes and H. Cheng, *Biophys J*, 1987, 52, 279-294.

16. M. Loeffler and B. Grossmann, *J Theor Biol*, 1991, 150, 175-191.

17. Y. Q. Li, S. A. Roberts, U. Paulus, M. Loeffler and C. S. Potten, *J Cell Sci*, 1994, 107 (Pt 12), 3271-3279.

18. M. Loeffler, T. Bratke, U. Paulus, Y. Q. Li and C. S. Potten, *J Theor Biol*, 1997, 186, 41-54.

19. D. Drasdo, *Phys Rev Lett*, 2000, 84, 4244-4247.

20. C. M. Edwards and S. J. Chapman, *B Math Biol*, 2007, 69, 1927-1942.

21. E. Hannezo, J. Prost and J. F. Joanny, *Phys Rev Lett*, 2011, 107, 078104.

22. M. R. Nelson, D. Howard, O. E. Jensen, J. R. King, F. R. Rose and S. L. Waters, *Biomech Model Mechanobiol*, 2011, 10, 883-900.

23. P. Buske, J. Przybilla, M. Loeffler, N. Sachs, T. Sato, H. Clevers and J. Galle, *FEBS J*, 2012, DOI: 10.1111/j.1742-4658.2012.08646.x.

24. T. Sato, D. E. Stange, M. Ferrante, R. G. Vries, J. H. Van Es, S. Van den Brink, W. J. Van Houdt, A. Pronk, J. Van Gorp, P. D. Siersema and H. Clevers, *Gastroenterology*, 2011, 141, 1762-1772.

25. T. Sato, R. G. Vries, H. J. Snippert, M. van de Wetering, N. Barker, D. E. Stange, J. H. van Es, A. Abo, P. Kujala, P. J. Peters and H. Clevers, *Nature*, 2009, 459, 262-U147.

26. A. Ootani, X. Li, E. Sangiorgi, Q. T. Ho, H. Ueno, S. Toda, H. Sugihara, K. Fujimoto, I. L. Weissman, M. R. Capecchi and C. J. Kuo, *Nat Med*, 2009, 15, 701-706.

27. T. Sato, J. H. van Es, H. J. Snippert, D. E. Stange, R. G. Vries, M. van den Born, N. Barker, N. F. Shroyer, M. van de Wetering and H. Clevers, *Nature*, 2011, 469, 415-+.

28. A. Durand, B. Donahue, G. Peignon, F. Letourneur, N. Cagnard, C. Slomianny, C. Perret, N. F. Shroyer and B. Romagnolo, *PNAS USA*, 2012, 109, 8965-8970.

29. C. Pin, A. J. Watson and S. R. Carding, *Plos One*, 2012, 7, e37115.

30. H. J. Snippert, A. G. Schepers, J. H. van Es, B. D. Simons and H. Clevers, *EMBO reports*, 2014, 15, 62-69.

31. C. S. Potten, *Philosophical Transactions of the Royal Society B-Biological Sciences*, 1998, 353, 821-830.

32. A. Hirata, J. Utikal, S. Yamashita, H. Aoki, A. Watanabe, T. Yamamoto, H. Okano, N. Bardeesy, T. Kunisada, T. Ushijima, A. Hara, R. Jaenisch, K. Hochedlinger and Y. Yamada, *Development*, 2013, 140, 66-75.

33. A. Humphries, B. Cereser, L. J. Gay, D. S. Miller, B. Das, A. Gutteridge, G. Elia, E. Nye, R. Jeffery, R. Poulsom, M. R. Novelli, M. Rodriguez-Justo, S. A. McDonald, N. A. Wright and T. A. Graham, *Proc Natl Acad Sci U S A*, 2013, 110, E2490-2499.

34. H. Cheng and M. Bjerknes, *Anat Rec*, 1985, 211, 420-426.

35. J. J. Dehmer, A. P. Garrison, K. E. Speck, C. M. Dekaney, L. Van Landeghem, X. F. Sun, S. J. Henning and M. A. Helmrath, *Plos One*, 2011, 6.

36. A. G. Cummins, A. G. Catto-Smith, D. J. Cameron, R. T. Couper, G. P. Davidson, A. S. Day, P. D. Hammond, D. J. Moore and F. M. Thompson, *J Pediatr Gastroenterol Nutr*, 2008, 47, 153-157.

37. M. R. Nelson, J. R. King and O. E. Jensen, *Mathematical biosciences*, 2013, 246, 229-241.

38. S. J. Dunn, A. G. Fletcher, S. J. Chapman, D. J. Gavaghan and J. M. Osborne, *J Theor Biol*, 2012, 298, 82-91.

39. D. Drasdo and M. Loeffler, *Nonlinear Analysis-Theory Methods & Applications*, 2001, 47, 245-256.

40. J. Berlanga-Acosta, R. J. Playford, N. Mandir and R. A. Goodlad, *Gut*, 2001, 48, 803-807.

41. O. Bashir, A. J. Fitzgerald, J. Berlanga-Acosta, R. J. Playford and R. A. Goodlad, *Clin Sci (Lond)*, 2003, 105, 323-330.

42. A. G. Cummins, B. J. Jones and F. M. Thompson, *Digest Dis Sci*, 2006, 51, 718-723.

43. A. Milicic, L. A. Harrison, R. A. Goodlad, R. G. Hardy, A. M. Nicholson, M. Presz, O. Sieber, S. Santander, J. H. Pringle, N. Mandir, P. East, J. Obszynska, S. Sanders, E. Piazuelo, J. Shaw, R. Harrison, I. P. Tomlinson, S. A. McDonald, N. A. Wright and J. A. Jankowski, *Cancer Res*, 2008, 68, 7760-7768.

44. J. K. Fauser, R. P. Donato, J. A. Woenig, S. J. Proctor, A. P. Trotta, P. K. Grover, G. S. Howarth, I. A. Penttila and A. G. Cummins, *J Pediatr Gastroenterol Nutr*, 2012, 55, 26-31.

45. P. Andreu, S. Colnot, C. Godard, S. Gad, P. Chafey, M. Niwa-Kawakita, P. Laurent-Puig, A. Kahn, S. Robine, C. Perret and B. Romagnolo, *Development*, 2005, 132, 1443-1451.

46. M. E. Rothenberg, Y. Nusse, T. Kalisky, J. J. Lee, P. Dalerba, F. Scheeren, N. Lobo, S. Kulkarni, S. Sim, D. Qian, P. A. Beachy, P. J. Pasricha, S. R. Quake and M. F. Clarke, *Gastroenterology*, 2012, 142, 1195-1205 e1196.

47. S. Roth, P. Franken, A. Sacchetti, A. Kremer, K. Anderson, O. Sansom and R. Fodde, *Plos One*, 2012, 7, e38965.

48. J. H. van Es, T. Sato, M. van de Wetering, A. Lyubimova, A. N. Nee, A. Gregorieff, N. Sasaki, L. Zeinstra, M. van den Born, J. Korving, A. C. Martens, N. Barker, A. van Oudenaarden and H. Clevers, *Nature cell biology*, 2012, 14, 1099-1104.

49. S. J. Buczacki, H. I. Zecchini, A. M. Nicholson, R. Russell, L. Vermeulen, R. Kemp and D. J. Winton, *Nature*, 2013, 495, 65-69.

50. H. Clevers, *Nature*, 2013, 495, 53-54.

51. M. Leushacke, A. Ng, J. Galle, M. Loeffler and N. Barker, *Cell*, 2013, 5, 1-8.

52. H. Miyoshi, R. Ajima, C. T. Luo, T. P. Yamaguchi and T. S. Stappenbeck, *Science*, 2012, 338, 108-113.

53. T. Sato, R. G. Vries, H. J. Snippert, M. van de Wetering, N. Barker, D. E. Stange, J. H. van Es, A. Abo, P. Kujala, P. J. Peters and H. Clevers, *Nature*, 2009, 459, 262-265.

54. N. Barker, J. H. van Es, J. Kuipers, P. Kujala, M. van den Born, M. Cozijnsen, A. Haegebarth, J. Korving, H. Begthel, P. J. Peters and H. Clevers, *Nature*, 2007, 449, 1003-U1001.

55. Q. S. Li, G. Y. Lee, C. N. Ong and C. T. Lim, *Biochem Biophys Res Commun*, 2008, 374, 609-613.

56. J. L. Hutter and J. Bechhoefer, *Rev Sci Instrum*, 1993, 64, 1868-1873.

57. F. A. Meineke, C. S. Potten and M. Loeffler, *Cell Proliferat*, 2001, 34, 253-266.

58. J. Galle, M. Hoffmann and G. Aust, *J Math Biol*, 2009, 58, 261-283.

59. P. Buske, J. Galle, N. Barker, G. Aust, H. Clevers and M. Loeffler, *PLoS computational biology*, 2011, 7, e1001045.

60. J. M. Osborne, A. Walter, S. K. Kershaw, G. R. Mirams, A. G. Fletcher, P. Pathmanathan, D. Gavaghan, O. E. Jensen, P. K. Maini and H. M. Byrne, *Philos T Roy Soc A*, 2010, 368, 5013-5028.

61. M. Loeffler, R. Stein, H. E. Wichmann, C. S. Potten, P. Kaur and S. Chwalinski, *Cell Tissue Kinet*, 1986, 19, 627-645.

62. M. Loeffler, C. S. Potten, U. Paulus, J. Glatzer and S. Chwalinski, *Cell Tissue Kinet*, 1988, 21, 247-258.

63. J. Pitt-Francis, P. Pathmanathan, M. O. Bernabeu, R. Bordas, J. Cooper, A. G. Fletcher, G. R. Mirams, P. Murray, J. M. Osborne, A. Walter, S. J. Chapman, A. Garny, I. M. M. van Leeuwen, P. K. Maini, B. Rodriguez, S. L. Waters, J. P. Whiteley, H. M. Byrne and D. J. Gavaghan, *Comput Phys Commun*, 2009, 180, 2452-2471.

Figure Legends

Figure 1. Fluorescent microscopy of small intestinal organoids undergoing budding events. Lgr5+ stem cells are labelled in green. Lysozyme granules in Paneth cells are in red and cell nuclei in blue. Yellow arrows point at Paneth and stem cells intermingling at the base of the crypts. Red arrows indicate the initiation of buds in regions where Paneth cells are located. Green arrows point at stem cells located in between Paneth cells.

Figure 2. Crypt fission in cultured murine small intestinal organoids. Budding is initiated in areas rich in Paneth cells (asterisk).

Figure 3. (A) Comparison of the Young's modulus measured by Atomic Force Microscopy (AFM) of Lgr5-eGFP positive stem cells (red lines) and Paneth cells identified visually as non-fluorescent large granular cells (black lines). The Young's modulus reflects cell stiffness. (B) AFM force approach and retract curves showing hysteresis characteristic to viscous material. Colour codes as in 3A.

Figure 4. Comparison between fission measurements in simulated crypts and in cultured organoids: (A) Observed (black bars; n=22 initial crypts) and simulated (red bars; n=30-40 initial crypts simulated during 12 days for each tested value of α) distributions for the time interval between successive budding processes per crypt. Plots show the results obtained with twelve values of the parameter α, from 0.1 to 2, which controls the force required to deform Paneth cells. (B) Square difference between the observed and simulated frequencies plotted in Figure 4A; the smallest difference was detected with α = 1.3. (C) Simulated probability of budding -within a 12 days period- of stem cells clusters surrounded by Paneth cells with several values for the parameter α and for cluster sizes of 1 (●), 2 (◊), 3 (+) and 4 (○) stem cells. (D) Percentage of clusters of stem cells surrounded by Paneth cells of size of 1 (●), 2 (◊), 3 (+) and 4 (○) stem cells in simulated crypts. (E-H) Schematic representation of the location of the cell centres on the ring of the crypt formed by stem, S, and Paneth, P, cells when (E) all cells are deformable stem cells; (F) Paneth and stem cells have the same viscoelastic behaviour and (G) Paneth cells are more resistant to deformation (α=1.3) than stem cells. The simulated location of cell centres occurs over a period of 20 days. For all hypotheses the duration of the stem cell division cycle is a normal distributed random variable with a mean value of 21.5 h and standard deviation of 2.15 h. Stem cells divide asynchronously. (H) Location of cell centres (dots) and cell boundaries (lines) at the beginning of the division cycle (discontinuous lines) of a

stem cell (marked with an asterisk) surrounded by Paneth cells and ~21 h later immediately before division (continuous lines) under the hypothesis that Paneth cells are more resistance to deformation (α=1.3).

Figure 5. (A) Observed (black bars; n=17) and simulated (red bars; n=89) distributions for the for the specific growth rate of the crypt length. (B) Observed (black) and simulated (red) migration curves of the secondary crypt along the length of the primary crypt expressed in percentage.

Figure 6. Appearance of a secondary crypt completely developed at the base of the original crypt without migrating upwards and which replaces the original crypt.

Figure 7. Simulated growth of the new crypt and migration along the original crypt: (A) Simulated distributions of the time for the secondary crypt to reach its final size and (B) to reach the top of the original crypt. (C) Distribution of the position of the secondary crypt when reaching the final size and (D) of the size -number of cells- of the secondary crypt when reaching the top of the original crypt.

Figure 8. Average proportions of each cell type during crypt fission. A) Proportion of stem and secretory cells and B) of proliferative cells and absorptive progenitors per crypt.

Figure 9. Predicting growth of the intestinal epithelium by crypt fission. The predicted number of crypts and cells in the newly formed tissue assumes that budding and fission always take place in a crypt when a stem cell is surrounded by Paneth cells.

Figure 10. Geometry of the viscoelastic behavior of cells within the crypt. The deformation of the external side of the cell can be monitored by measuring the deformation of either the central vertical, i, or central horizontal, ii, axis. The pressure per unit length, P, derives from the difference between cell size and available space and it is uniformly applied to the external edge of a cell of width equal to $2R$. The length of the cell external edge is equal to L. v_y is the velocity of the flow in the Y direction.

Supplementary data

Table S1. Individual based model parameters

Figure S1. Frequency of cell velocities (cell positions/h) along the crypt during index reassignment process, i.e. moving to the ring immediately above (blue columns), and during time intervals in which cells do not change rings (red columns). Velocities are estimated in the three-dimensional space (A) as well as in each of the dimensions, Z (B), X (C) and Y (D). Velocities were estimated from 14.000 cells located in the upper half of a simulated crypt during one week. Numbers represent the average velocities and their standard errors for each group of cells according to colour.

Figure S2. Comparison of the theoretical velocity derived from the balance of forces within the crypt and the simulated velocity in our model. The difference between the theoretical and simulated velocity was measured in 40,000 cells evolving in a simulated crypt during one week. Blue columns represent velocity frequencies for cells undertaking index reassignment and therefore moving to the ring immediately above, while red columns are for cells that do not change ring. Numbers represent the average velocities for each group of cells according to colour.

Figure S3. Longitudinal view of a simulated fission event. The white arrow marks the initial location of the bud in the primary crypt at the time of fission initiation. The bud grows into a crypt that migrates upwards the primary crypt in the following days. The lumen (red) of both crypts is connected during this process.

Video S1. Simulation of a crypt fission event. Cells are represented by spherical shapes unrelated to the modelled cell shape.

Video S2. Simulation of a crypt fission event coupled with the observation of a crypt undergoing fission in a cultured organoid - period of observation is 1.2 days. Cells are represented by spherical shapes unrelated to the modelled cell shape.

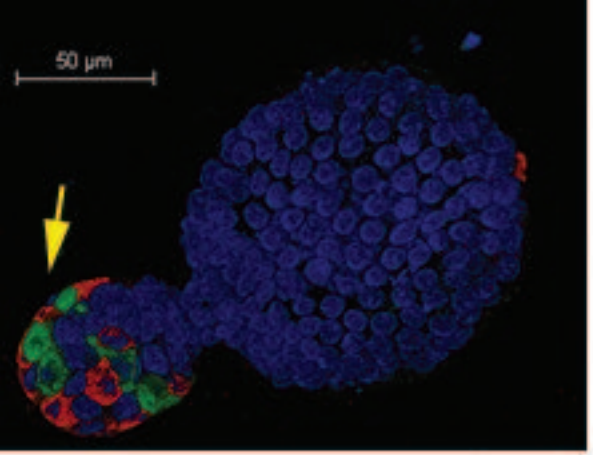

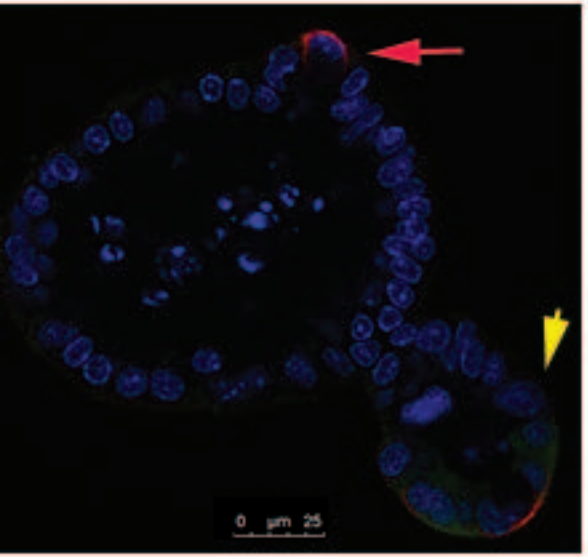

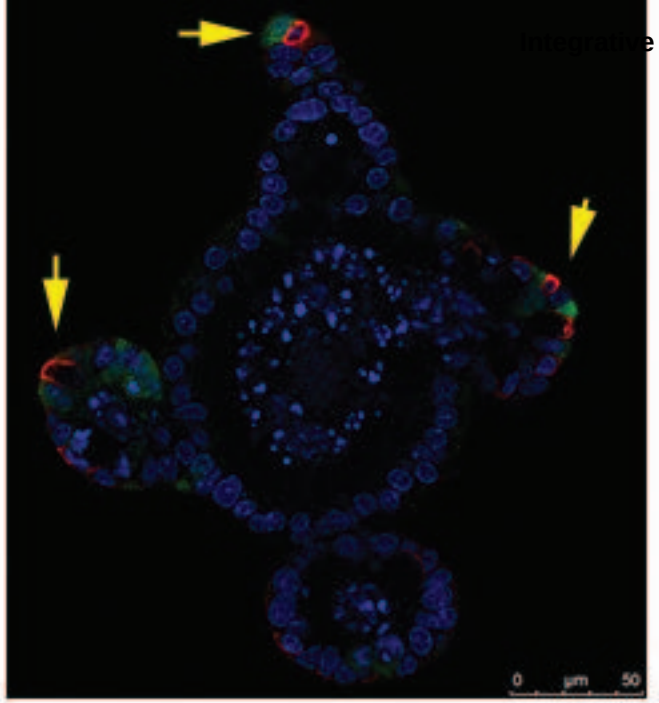

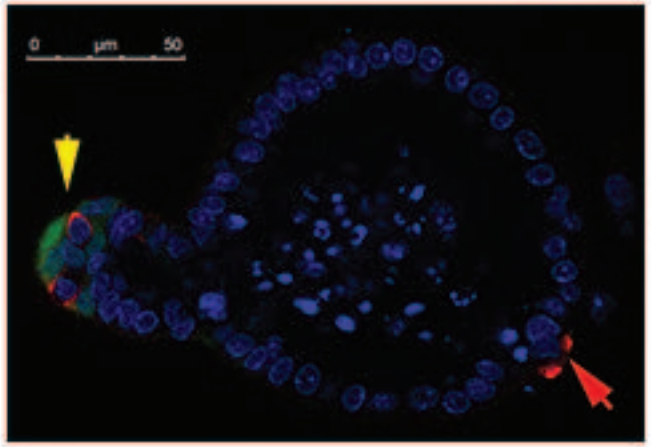

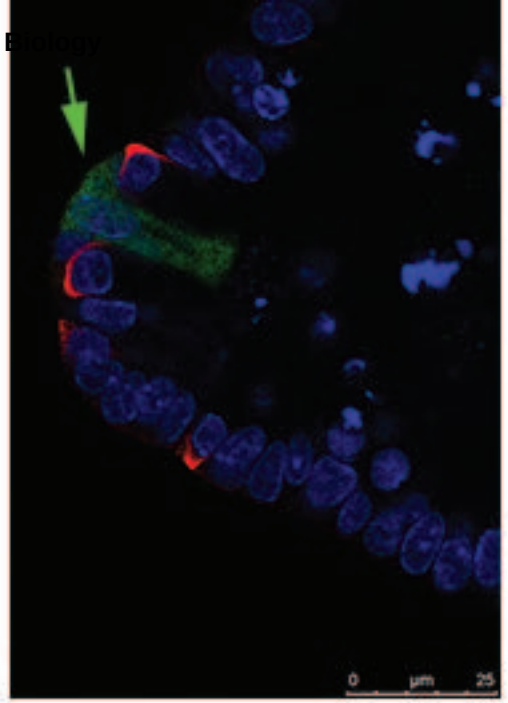

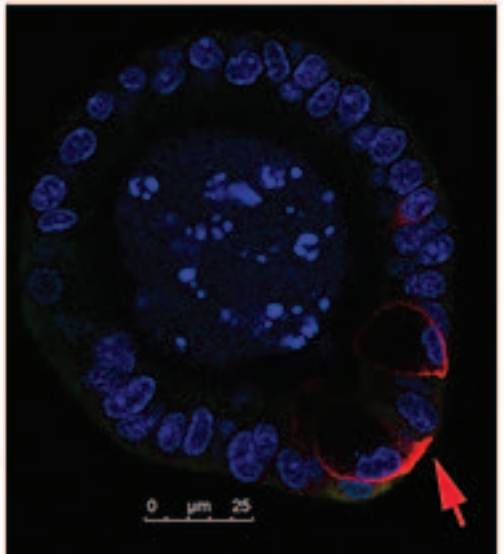

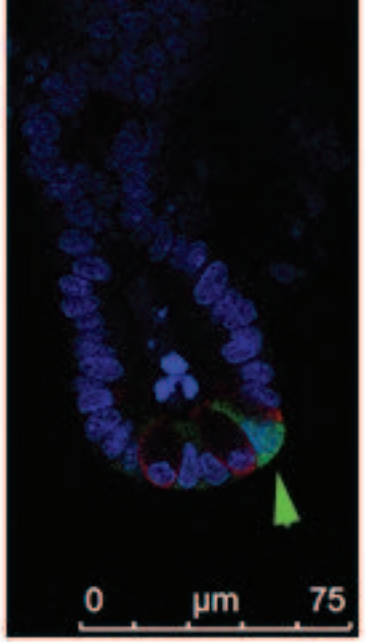

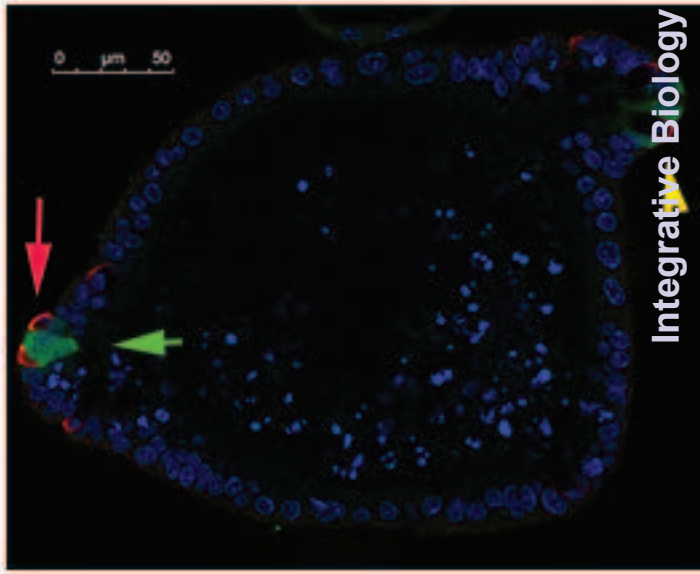

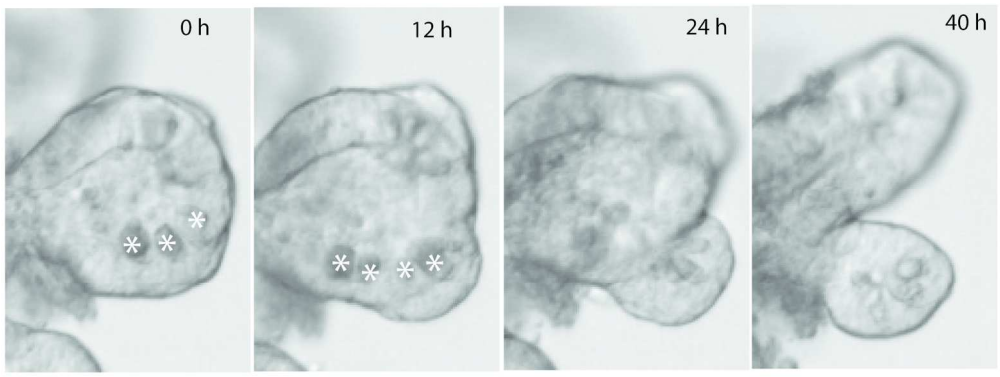

179x66mm (300 x 300 DPI)

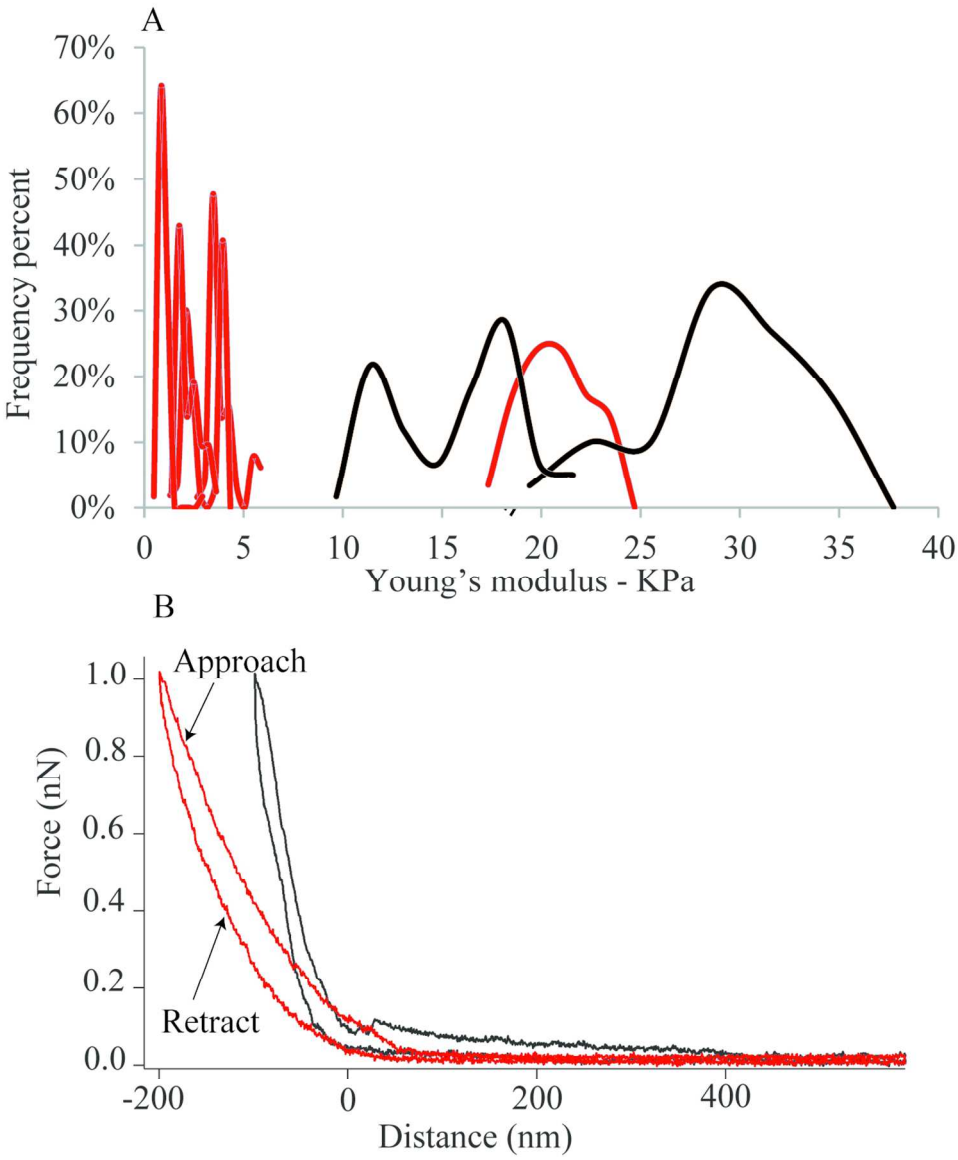

123x148mm (300 x 300 DPI)

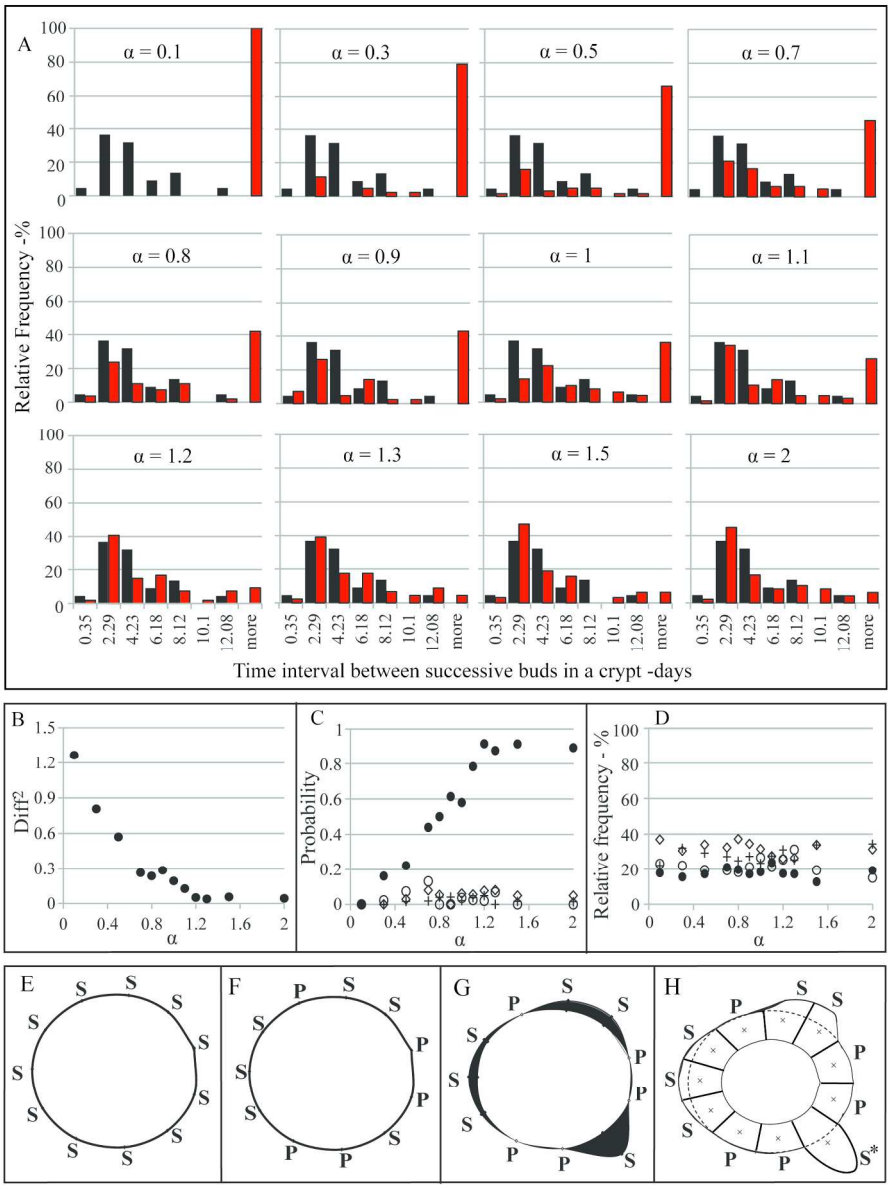

182x243mm (300 x 300 DPI)

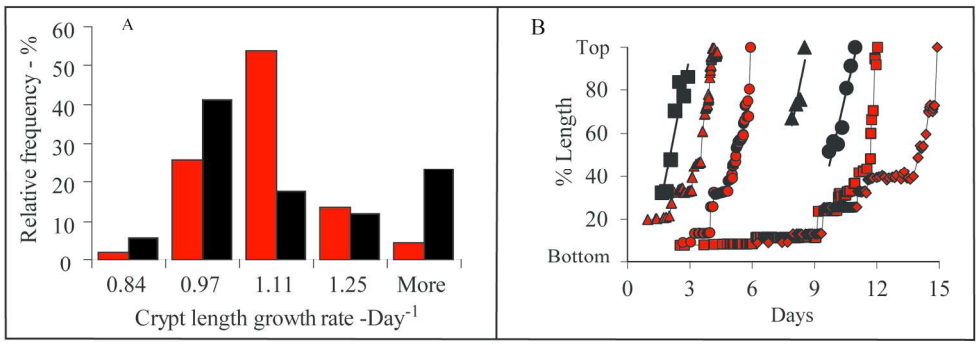

185x67mm (300 x 300 DPI)

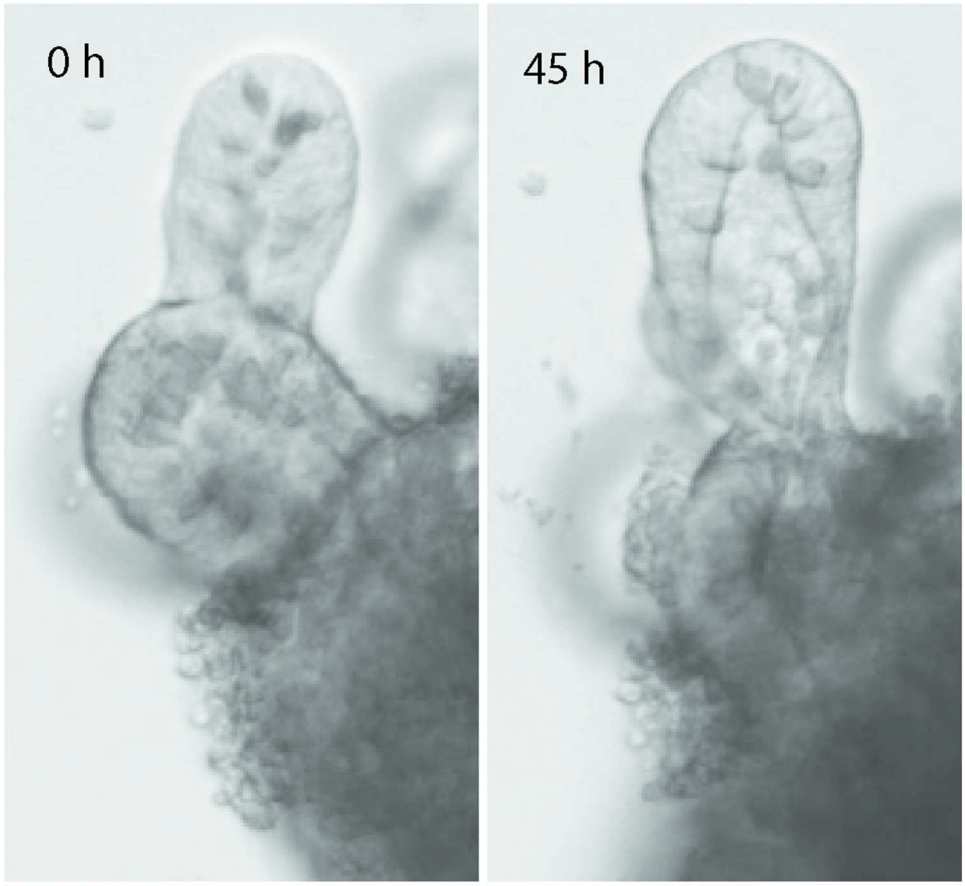

90x82mm (300 x 300 DPI)

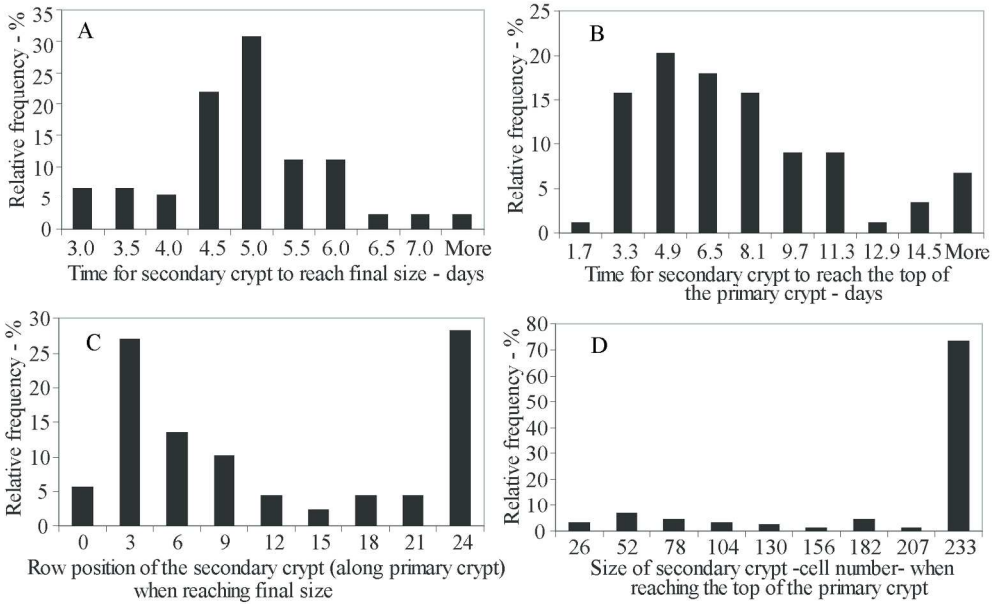

180x109mm (300 x 300 DPI)

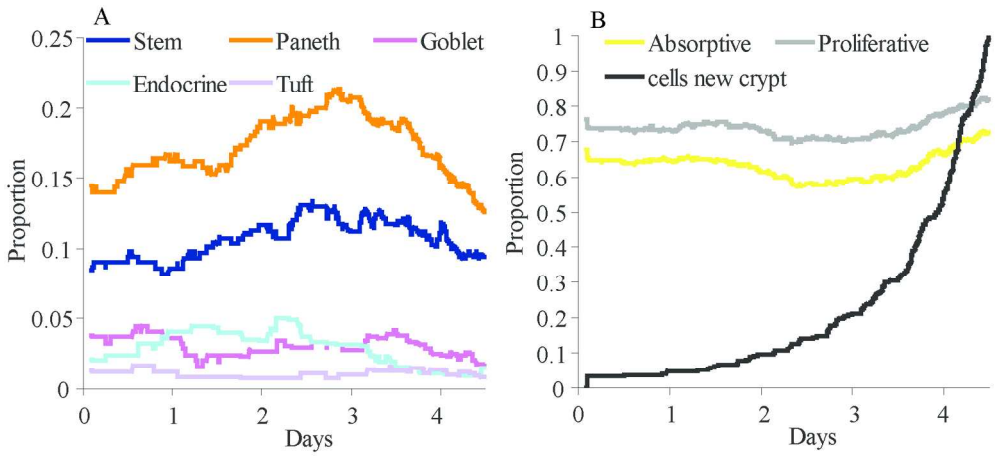

172x78mm (300 x 300 DPI)

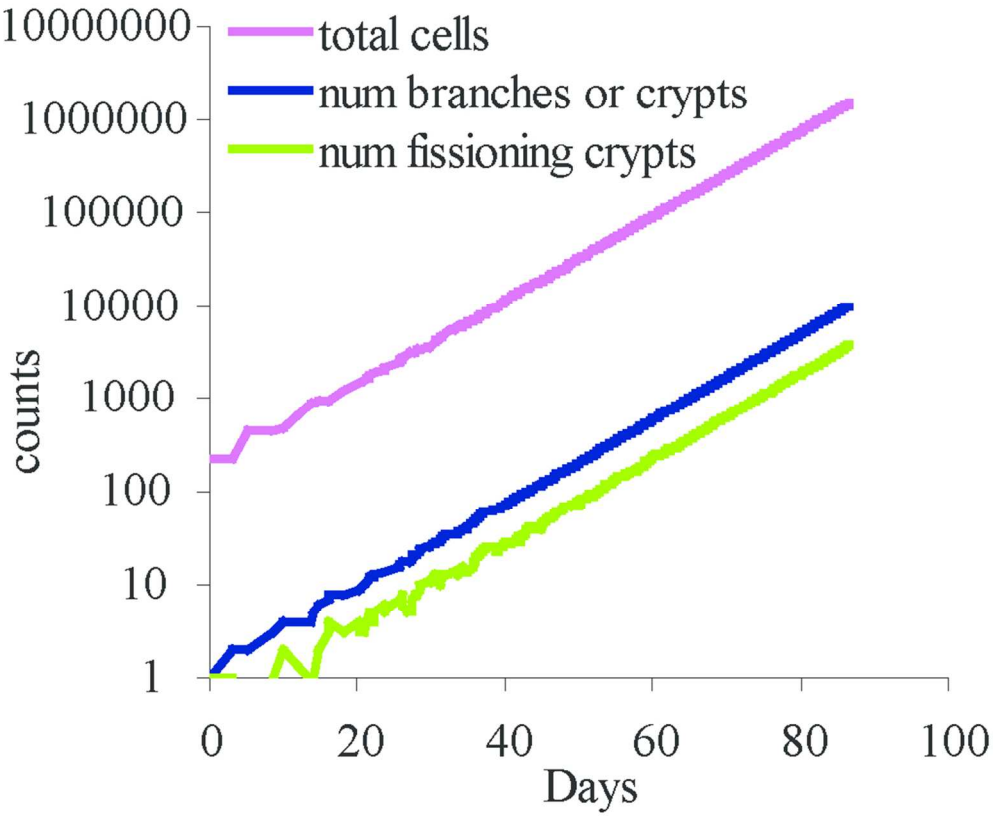

87x71mm (300 x 300 DPI)

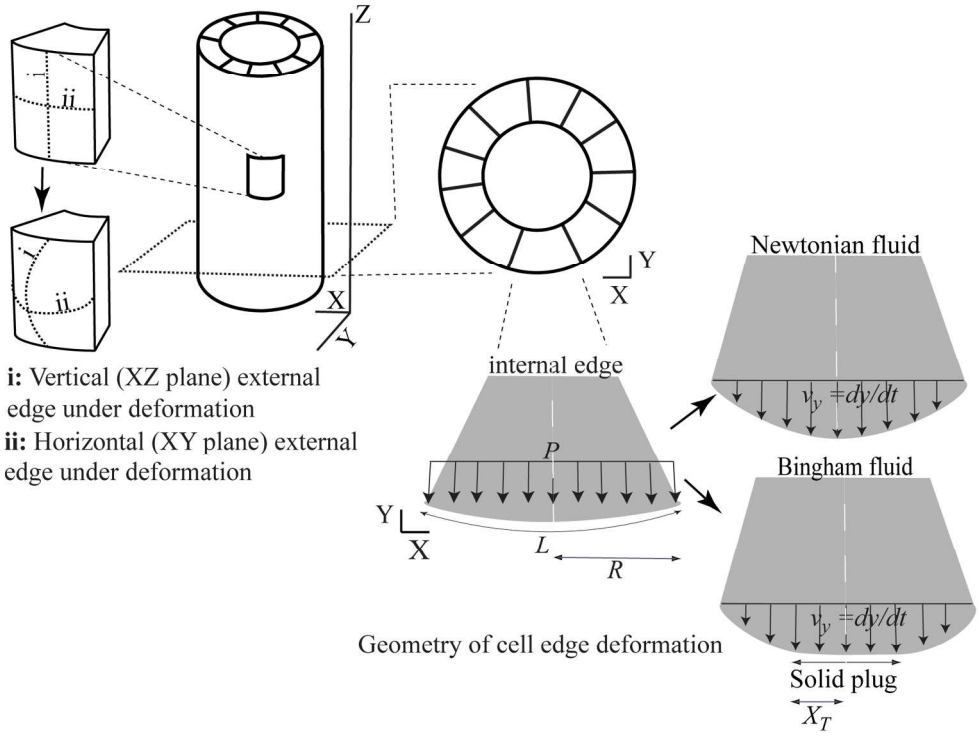

Geometry of cell edge deformation

163x123mm (300 x 300 DPI)